RSC Advances

PAPER

View Article Online
View Journal | View Issue

Cite this: *RSC Adv.*, 2026, **16**, 16865

Surface engineering of SnO_2 for improved perovskite/SnO_2 photodetectors

Jing Cai,[a] Guipeng Li,[b] Yulong Ying,[c] Hongping Li,*[d] Ahmad Fairuz Omar,[a] Marzaini Rashid*[a] and Mingming Chen*[b]

Received 31st December 2025
Accepted 20th March 2026

DOI: 10.1039/d5ra10121b

rsc.li/rsc-advances

Lead halide perovskite (LHP) heterojunctions have proven to be promising for achieving low-cost and efficient photodetection. However, the remarkable interfacial non-radiative recombination severely deteriorated the performance of the resulting devices. Herein, surface engineering of SnO_2 with ammonium tetrathiotungstate ($(NH_4)_2WS_4$) has been proposed to effectively passivate the interfacial defects at the LHP $CH_3NH_3PbI_3/SnO_2$ interface to fabricate high-performance photodetectors (PDs). Experimental and theoretical studies showed that the surface engineering with $(NH_4)_2WS_4$ resulted in S substituting for oxygen lattice of SnO_2, which passivated the surface oxygen vacancies of SnO_2. Further studies have shown that the S atoms at the surface of SnO_2 further suppressed the I vacancies and Pb vacancies at the bottom surface of $CH_3NH_3PbI_3$. Finally, improved $CH_3NH_3PbI_3/SnO_2$ PDs with the responsivity and detectivity of 0.41 A W^{-1} and 5×10^{12} Jones, respectively, at zero bias, have been demonstrated. The results presented in this work provide promising pathways to effectively passivate the interfacial defects of LHP/SnO_2 heterojunctions for achieving efficient photodetection in the future.

Introduction

Photodetectors (PDs), which can directly convert photons into electrical charge, are a fundamental component of various modern photodetection and imaging systems, such as digital imaging and hyperspectral sensing.[1–5] Recently, halide lead perovskites (LHPs) (ABX_3, where A is $CH_3NH_3^+$ (MA^+), $HC(NH_2)_2^+$ (FA^+); B is the Pb^{2-}; X is the Cl^-, Br^-, and I^-) have attracted tremendous attention in the optoelectronics community because of their superior optoelectrical properties including high absorption coefficient, long charge carrier diffusion length, and long charge carrier lifetime.[6] Benefiting from these advantages, LHPs have been regarded as potential candidates for realizing low-cost and efficient light harvesting and photodetection.[7] Notably, various kinds of LHP PDs, including narrowband, broadband, and wavelength-selective PDs, have been fabricated recently.[8,9] Benefiting from various advantages, such as a combination of optoelectrical properties of both semiconductors and being free from the need for controlled n- and p-type doping of specific materials,[10–13] LHP heterojunctions fabricated by preparing LHP and a different semiconductor in sequence have been considered as essential building blocks for fabricating efficient and cost-effective self-powered PDs.[14,15]

Recently, the rapid progresses of power conversion efficiency of LHP solar cells have motivated the explorations of advanced carrier transport layers.[16] It is worth noting that wide bandgap semiconductor tin oxide (SnO_2) has been widely employed to fabricate efficient LHP solar cells recently, benefiting from its high electron mobility, deep conduction band, and low-temperature processabilities.[17] Meanwhile, the construction of efficient PDs based on various LHP/SnO_2 heterojunctions has been further explored.[18] Similar to light harvesting, efficient photodetection can be readily achieved through a combination of the efficient absorption of photons and the efficient collection of excess carriers. Benefiting from ion doping-assisted suppression of point defects and seed layer-assisted nucleation-induced suppression of grain defects, the bulk defects of LHP thin films have been remarkably suppressed.[19,20] However, the interfacial defects induced non-radiative recombination have severely lowered the efficiency of carrier collection, greatly limiting the performance of LHP/SnO_2 heterojunction PDs.[21,22] In general, the interfacial defects consist of the surface defects of the buried layer and the deposited layer. In the case of the LHP/SnO_2 heterojunctions, the SnO_2 thin films prepared with various techniques have suffered from the natural surface oxygen vacancies (V_Os).[22] In addition, halide vacancies and lead vacancies have been evidenced at the bottom surface of LHPs owing to the weak bonding between LHPs and SnO_2.[23] It has been widely reported

[a]*School of Physics, Universiti Sains Malaysia, 11800 USM, Penang, Malaysia. E-mail: marzaini@usm.my*

[b]*Department of Microelectronics, Jiangsu University, Zhenjiang, Jiangsu 212013, China. E-mail: andychain@live.cn*

[c]*School of Materials Science and Engineering, Zhejiang Sci-Tech University, Hangzhou, 310018, China*

[d]*School of Materials Science and Engineering, Jiangsu University, Zhenjiang, Jiangsu 212013, China. E-mail: hpli@ujs.edu.cn*

that both surface defects deteriorated the performance of LHP/SnO_2 heterojunction devices.[24] Very recently, a great amount of effort has been devoted to suppressing the interfacial defects for fabricating improved LHP/SnO_2 heterojunction PDs.[25] However, the existing literatures mostly focused on either passivating the surface V_Os of SnO_2 thin films or suppressing the halide vacancies and lead vacancies at the bottom surface of LHPs.[26,27] For example, inorganic dielectric layers have been employed to passivate the surface V_Os of SnO_2 thin films.[28] Besides, various organic groups have been explored, but mainly suppress the halide vacancies and lead vacancies at the bottom surface of LHP thin films.[29] Practically, effective suppression of surface defects of both materials is fundamental for improving the performance of LHP/SnO_2 heterojunction PDs, while the related studies have seldom been reported so far.

Herein, surface engineering of SnO_2 with ammonium tetrathiotungstate ($(NH_4)_2WS_4$) has been proposed to realize an effective suppression of surface V_Os of SnO_2 and iodine vacancies (V_I) and lead vacancies (V_{Pb}) at the bottom surface of $MAPbI_3$. It has been shown that the surface V_Os of SnO_2 were effectively passivated *via* the sulfur (S) substitution for oxygen (O) lattice. In addition, the S atoms at the surface of SnO_2 further suppressed the V_I and V_{Pb} defects at the bottom surface of $MAPbI_3$. Collectively, performance-improved $MAPbI_3/SnO_2$ PDs with the responsivity and detectivity as high as 0.41 A W^{-1} and 5×10^{12} Jones, respectively, at the zero bias, have been demonstrated.

Results and discussions

The $MAPbI_3/SnO_2$ PDs were fabricated by spin-coating SnO_2 and $MAPbI_3$ thin films in sequence on an ITO substrate (Fig. 1a) (see experiments in SI for details). The treatment of surface engineering of SnO_2 was realized by adding $(NH_4)_2WS_4$ into SnO_2 aqueous solution, where the surface V_Os of SnO_2 were passivated through the S substitution during stirring. The morphological and structural properties of samples were characterized by scanning electron microscopy (SEM) and X-ray diffraction (XRD) techniques. The suppression of surface V_O defects in SnO_2 and V_{Pb} of $MAPbI_3$ has been verified through steady-state and transient photoluminescence (PL), X-ray photoelectron spectroscopy (XPS) characterizations, and density functional theory (DFT) calculations.

Structure and elements analysis have confirmed the crystallization of SnO_2 after spin-coating of pure SnO_2 and SnO_2/$(NH_4)_2WS_4$ aqueous solutions (Fig. S1–S2, SI). Fig. 1b and c show the typical SEM images of SnO_2 and S-SnO_2 thin films. It shows that the S-SnO_2 thin films exhibit an improved morphology in terms of improved compactness and uniformity, while the SnO_2 thin films show a rough surface with notable gaps. This suggests that the $(NH_4)_2WS_4$ additive benefits the preparation of high-quality SnO_2 thin films from nanoparticles. Due to the small thickness and limited resolution of the SEM technique, the thickness of SnO_2 and S-SnO_2 thin films was not obtained, but has been estimated as ~10 nm from the previous reports.[30] Notably, the compact and uniform morphology of S-SnO_2 thin films exhibits a reduction of carrier scattering effect. As revealed from current–voltage (*I–V*) measurements (Fig. S3, SI), the S-SnO_2 thin films feature a reduced resistivity. As a result, the carrier collection at the $MAPbI_3/SnO_2$ interfaces is expected to be improved.

Fig. 1d–g present the SEM images of $MAPbI_3$ thin films spin-coated on SnO_2 and S-SnO_2 thin films. As shown, both samples exhibit a similar morphology with comparable grain size, compactness, and thickness. Specifically, the grain sizes and thickness of both samples were characterized as around 450 ± 32 nm (Fig. 1d and e) and 230 nm (Fig. 1f and g), respectively. This suggests that surface engineering of SnO_2 with $(NH_4)_2WS_4$ seems not to influence the growth processes of $MAPbI_3$ thin films.

Structural and optical properties measurements were carried out to further compare the quality of $MAPbI_3$ thin films prepared on SnO_2 and S-SnO_2 thin films, and the results are shown in Fig. 2. It shows that both $MAPbI_3$ thin films exhibit similar XRD patterns (Fig. 2a), which can be indexed into the orthorhombic phase. Careful analysis shows that both $MAPbI_3$ thin films exhibit similar crystalline quality from the XRD peaks' positions and full width at half maximums (FWHMs, Table S1, SI). Such a claim can be supported from small differences in their steady and transient PL spectra (Fig. 2b). As shown, the PL intensity and carrier recombination processes of both $MAPbI_3$ thin films are almost same. Collectively, surface engineering with the $(NH_4)_2WS_4$ has improved the morphology of SnO_2 thin films, while it has neglected roles in subsequent crystallization of $MAPbI_3$ thin films.

To verify the suppression of surface V_Os, XPS measurements on the SnO_2 thin films were performed. Notably, the XPS method has shown strong effectiveness in analyzing surface chemical composition.[31,32] Fig. 3a illustrates the core-level spectra of O 1s of SnO_2 and S-SnO_2 thin films. Both spectra can be fitted into three peaks (peak I, II, and III), which correspond to various states of O at the SnO_2 surface. As can be seen, the binding energies are observed at 530.5 eV, 531.3 eV, and 532.0 eV, which can be attributed to lattice O, V_O, and adsorbed oxhydryl (OH^-), respectively.[33] Notably, the concentration of various components can be semiquantitatively evaluated from the relative intensities of corresponding XPS peaks.[33] Accordingly, it can be concluded that S-SnO_2 thin films show a reduced surface V_O from the decreased intensity of peak II compared to SnO_2 thin films. Further observations suggest that the reduction of surface V_Os is probably caused by the S substituting for O in S-SnO_2 thin films. On the one hand, a remarkable peak can be observed in S 2p XPS spectrum (Fig. 3b), which verifies the successful doping of S in S-SnO_2 thin films. On the other hand, the binding energies of Sn 3d in S-SnO_2 thin films redshift by around 0.3 eV compared to those in SnO_2 thin films (Fig. 3c). This is attributed to the increased electron density around Sn atoms,[34] which well correlates to the formation of the Sn–S bond in the current situation.

The above observations indicate that interface engineering with $(NH_4)_2WS_4$ resulted in a doping of S atoms, which suppressed the surface V_Os in S-SnO_2 thin films. However, it is difficult to reveal the doping processes at this stage, but can be expected as follows:

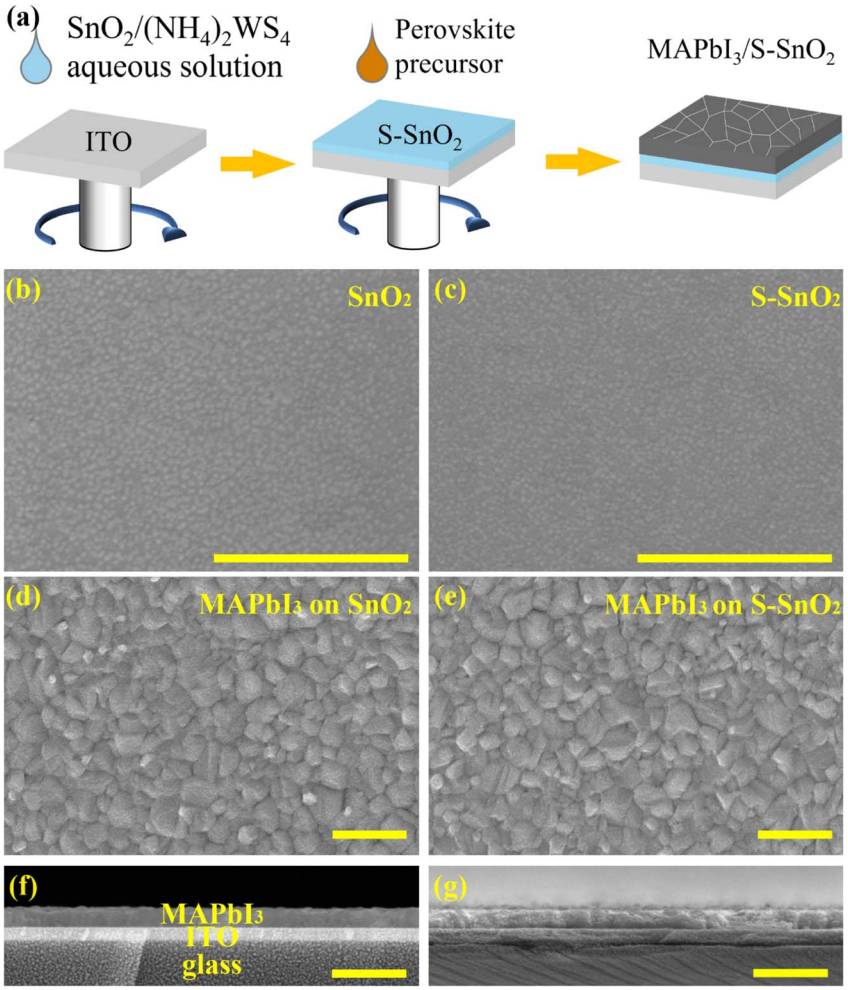

Fig. 1 Morphology of SnO_2 and $MAPbI_3$ thin films. (a) Scheme of experimental details for preparing $MAPbI_3$/S-SnO_2 heterojunctions. SEM images of (b) SnO_2, (c) S-SnO_2, (d and f) $MAPbI_3$ thin films grown on SnO_2, and (e and g) $MAPbI_3$ thin films grown on S-SnO_2.

$$SnO_2\_V_O + S \rightarrow SnO_2\_S_O$$

where $SnO_2\_V_O$ is the SnO_2 with a surface V_O, $SnO_2\_S_O$ is the SnO_2 with S substituting for O lattice. Herein, to better understand the mechanisms of suppression of surface V_Os by S doping, DFT calculations were carried out. As reported before, the probability of S substitution for surface O lattice (S_O) can be revealed from their formation energies (ΔE),[35] which can be calculated from the eqn (1):

$$\Delta E(SnO_2\_S_O) = E(SnO_2\_S_O) - [E(SnO_2\_V_O) + E(S)] \quad (1)$$

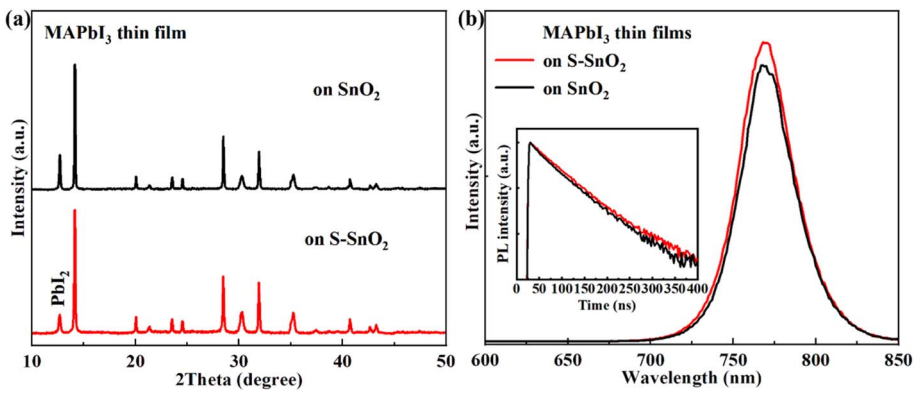

Fig. 2 Structural and optical properties of $MAPbI_3$ thin films grown on SnO_2 and S-SnO_2. (a) XRD and (b) PL. The inset in (b) shows the TRPL.

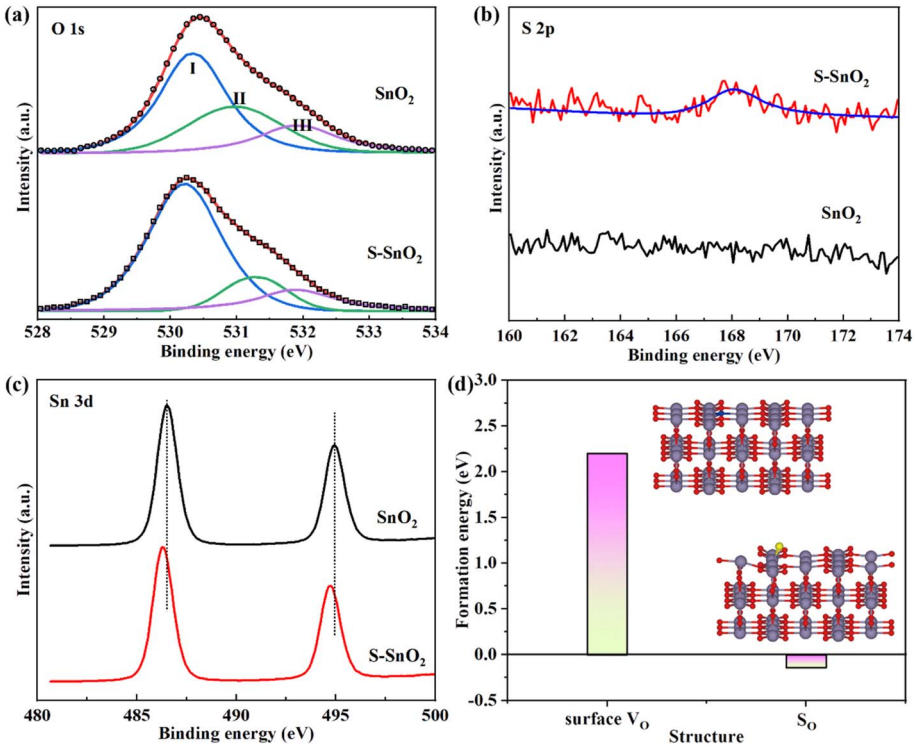

Fig. 3 Passivation of surface V_Os of SnO_2 by S atoms. (a–c) XPS data of (a) O, (b) S, and (c) Sn atoms. (d) Formation energies of surface V_Os and S substituting for O of SnO_2. The inset in (d) indicates the corresponding supercells, where red, gray, blue, and yellow balls are O, Sn, V_O, and S, respectively.

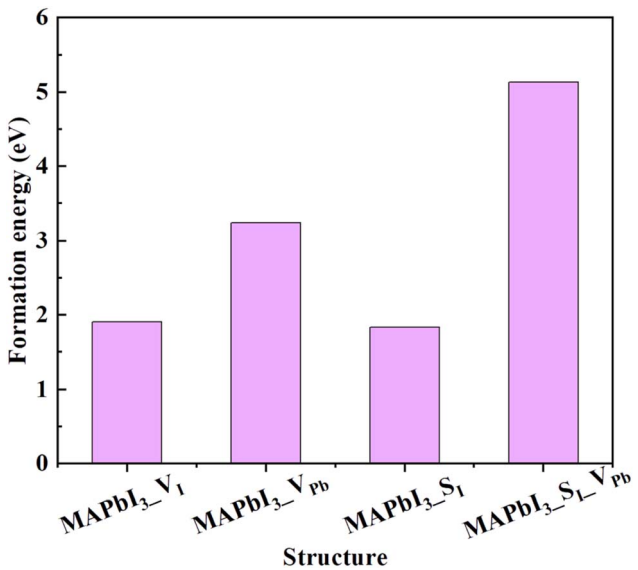

Fig. 4 Formation energies of V_I, V_{Pb}, S substituting for I, and S substituting for I with a V_{Pb} nearby of $MAPbI_3$. The corresponding supercells are depicted in Fig. S4 (SI). The formation energies were calculated using formulas similar to eqn (1).

where $E(SnO_2\_S_O)$, $E(SnO_2\_V_O)$, and $E(S)$ are the total energies of the supercell with S substitution for surface O and that with a surface V_O, and the energy of individual S atom, respectively. The formation energy of $SnO_2\_V_O$ structure ($\Delta E(SnO_2\_V_O)$) was calculated with a similar scenario. Fig. 3d depicts the formation energies of SnO_2 with a surface V_O and S substitution for surface O. It can be seen that the formation energy of surface V_O is as high as 2.198 eV. This suggests that the high-density surface V_O (Fig. 3a) cannot be related to thermodynamic effects, but might be attributed to mechanical effects between the nanoparticles or hydrogen bonding in the solvent environment. Notably, the formation energy of S substitution for surface O was calculated as low as −0.141 eV. This shows that the S_O structure is thermally preferred, which demonstrates the effective suppression of surface V_Os of SnO_2 through the surface engineering with the $(NH_4)_2WS_4$.

It has been noticed that S atoms on the SnO_2 surface showed a strong electrostatic interaction with Pb ions of $MAPbI_3$ compared to O of SnO_2.[36] In this case, the interfacial S atoms are expected to fill the V_I and further suppress the formation of V_{Pb} at the bottom surface of $MAPbI_3$ thin films. Since the small penetration depth of X-ray, the local chemical states of Pb and I atoms at the $MAPbI_3/SnO_2$ interface cannot be experimentally explored from XPS techniques. To demonstrate the hypotheses, the formation energies of $MAPbI_3$ with a V_I ($MAPbI_3\_V_I$), $MAPbI_3$ with a V_{Pb} ($MAPbI_3\_V_{Pb}$), $MAPbI_3$ with a S atom substituting for I lattice ($MAPbI_3\_S_I$), and $MAPbI_3\_S_I$ with a V_{Pb} nearby S ($MAPbI_3\_S_I\_V_{Pb}$) (Fig. S4, SI) were calculated, and the results are provided in Fig. 4. It shows that the $MAPbI_3\_S_I$ structure shows a reduced formation energy (1.84 eV) compared to $MAPbI_3\_V_I$ (1.91 eV), and the $MAPbI_3\_S_I\_V_{Pb}$ exhibits a reduced formation energy (3.25 eV) compared to $MAPbI_3\_V_{Pb}$

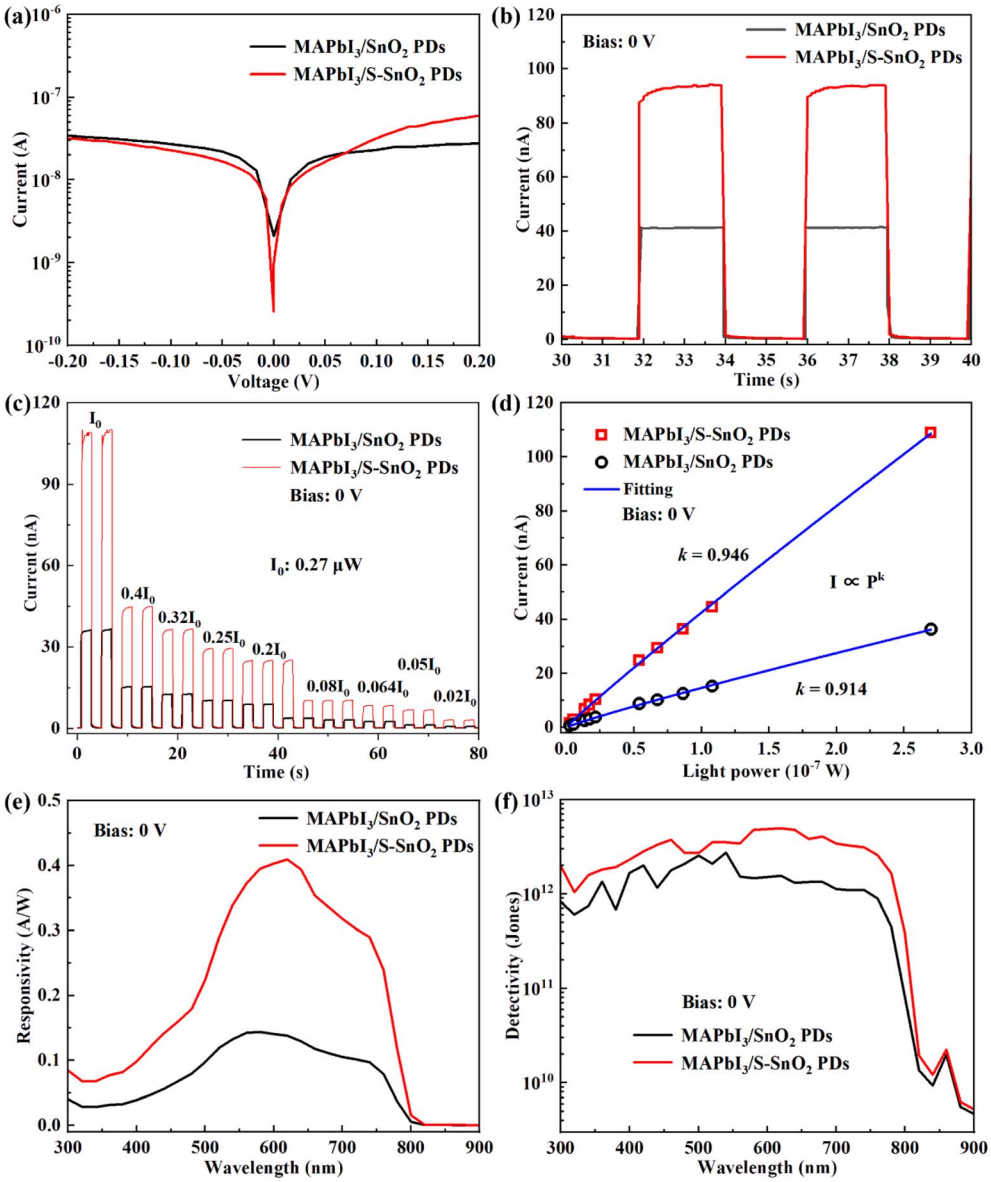

Fig. 5 Performance of $MAPbI_3/SnO_2$ PDs. (a) *I*–*V* curves captured in dark. (b) *I*–*t* curves captured under pulsed illumination. (b and c) *I*–*t* curves and photocurrent captured under different light powers. Data in d were extracted from c. (e) Responsivity. (f) Detectivity.

(5.14 eV). This suggests that the S atoms at the surface of SnO_2 thin films have remarkable potential to suppress the V_I and V_{Pb} defects at the bottom surface of $MAPbI_3$ thin films.

After sputtering Au electrodes, $MAPbI_3/SnO_2$ heterojunction PDs were fabricated (Fig. S5, SI). As shown in Fig. S6 (SI), among various concentrations, engineering SnO_2 NPs with 1.0 mg mL^{-1} of $(NH_4)_2WS_4$ produced the optimal $MAPbI_3$/S-SnO_2 PDs, resulting in the highest photocurrent. Accordingly, the performance of $MAPbI_3$/S-SnO_2 PDs, prepared with 1.0 mg mL^{-1} $(NH_4)_2WS_4$ engineering, is examined in detail below. Fig. 5a illustrates the *I*–*V* curves of $MAPbI_3/SnO_2$ and $MAPbI_3$/S-SnO_2 PDs captured in the dark. It shows that the $MAPbI_3$/S-SnO_2 PDs exhibit reduced current under reverse bias and reduced turn-on voltage under forward bias. As shown in Fig. 1 and 2, the $MAPbI_3$ thin films prepared on SnO_2 and S-SnO_2 exhibit a similar crystalline quality. Thus, the reduced reverse current and turn-on voltage can be attributed to the suppression of interfacial defects at the $MAPbI_3$/S-SnO_2 interface, as discussed above.

Fig. 5b shows the current–time (*I*–*t*) curves of $MAPbI_3/SnO_2$ and $MAPbI_3$/S-SnO_2 PDs at zero bias with 540 nm illumination switched on and off. It can be seen that both devices show excellent on-off switching performance. Notably, the $MAPbI_3$/S-SnO_2 PDs show an improved photocurrent, which increased by around 2.2 times compared to $MAPbI_3/SnO_2$ PDs. According to above discussions, this should be caused by the suppressed interfacial non-radiative recombination at $MAPbI_3$/S-SnO_2 interfaces. Further studies suggest that both devices exhibit nearly a linear response to light power. As shown in Fig. 5c and d, the photocurrents of $MAPbI_3/SnO_2$ and $MAPbI_3$/S-SnO_2 PDs nearly scale linearly with light power from 10^{-9} W to 10^{-7} W,

Table 1 Comparison of photodetection performance of $MAPbI_3/SnO_2$ heterojunction PDs and related devices reported before

Device	Bias (V)	Responsivity (A/W)	Detectivity (Jones)	Ref.
Spiro-OMeTAD/$FAPb(I/Br)_3/SnO_2$	1.0	0.0438	3.56×10^{13}	37
Spiro-OMeTAD/$MAFAPb(Br/I)_3/SnO_2$	1.0	0.0722	4.67×10^{13}	38
$SnO_2/MAPbI_3/MoO_3$	0	0.0509	2.23×10^{12}	39
$CsCu_2I_3$/GaN	0	0.10634	9.24×10^{11}	40
$MAPbI_3$/ZnO	7	2.73	1.09×10^{12}	41
$C_{60}/MAPbI_3$/GaN	0	0.198	7.96×10^{12}	42
$TiO_2/MAPbI_3$	−0.8	0.405	2.07×10^{11}	43
PEDOT:PSS/$MAPbI_3$/PTB7-Th:COTIC-4F	−0.5	0.58	1.64×10^{12}	44
$MAPbI_3/SnO_2$@r-$PMo_{11}V$	3	0.039	9.3×10^{10}	45
$MAPbI_3$/S-SnO_2	0	0.41	4.6×10^{12}	This work

suggesting that $MAPbI_3/SnO_2$ heterojunction PDs can be used to detect the light power.

The performance of $MAPbI_3/SnO_2$ and $MAPbI_3$/S-SnO_2 PDs is further studied from the responsivity and detectivity, and the results are shown in Fig. 5c and d. As reported before, the responsivity (R) and detectivity (D^*) can be calculated from eqn (2) and (3) provided below:

$$R = \frac{I_{ph} - I_{dark}}{P \times S} \quad (2)$$

$$D^* = \frac{R}{\sqrt{2eI_{dark}/S}} \quad (3)$$

where I_{ph} and I_{dark} are the photocurrent and dark current, P is the light power density (in W cm^{-2}), S is the device area (the area of the top Au electrode, 0.01 mm^2), e is the electric charge (1.6×10^{-19} C). As depicted in Fig. 5e and f, the photoresponsivity and detectivity of $MAPbI_3/SnO_2$ PDs are 0.14 A W^{-1} and 2×10^{12} Jones, respectively, at the zero bias, which increased by around 2.9 times (0.41 A W^{-1}) and 2.3 times (4.6×10^{12} Jones) for $MAPbI_3$/S-SnO_2 PDs. The improved photodetection performance of $MAPbI_3$/S-SnO_2 PDs is mainly attributed to the suppressed interfacial non-radiative recombination, which benefits from the effective interfacial passivation induced by the surface engineering with $(NH_4)_2WS_4$ as evidenced above. Table 1 summarizes a comparison of the photodetection performance of the $MAPbI_3$/S-SnO_2 PDs shown herein and related PDs reported before, highlighting the critical roles of surface engineering with $(NH_4)_2WS_4$ in improving the performance of $MAPbI_3/SnO_2$ heterojunction PDs.

Further studies reveal that surface engineering of SnO_2 with $(NH_4)_2WS_4$ improved the stability of photodetection. As shown in Fig. 6a and b, the photocurrent of $MAPbI_3/SnO_2$ PDs decreases to 85% of the initial value under pulsed illumination (Fig. 6a) and 60% under steady illumination (Fig. 6b) over 3600 s. In comparison, the photocurrent slightly decreases (2% and 10%) in $MAPbI_3$/S-SnO_2 PDs. Generally, the interfacial non-radiative recombination induces substantial thermal effects under illumination,[46] which account for the inferior stability observed in $MAPbI_3/SnO_2$ PDs. Thus, the improved stability of photodetection of $MAPbI_3$/S-SnO_2 mainly benefits from the effective interfacial passivation as discussed above.

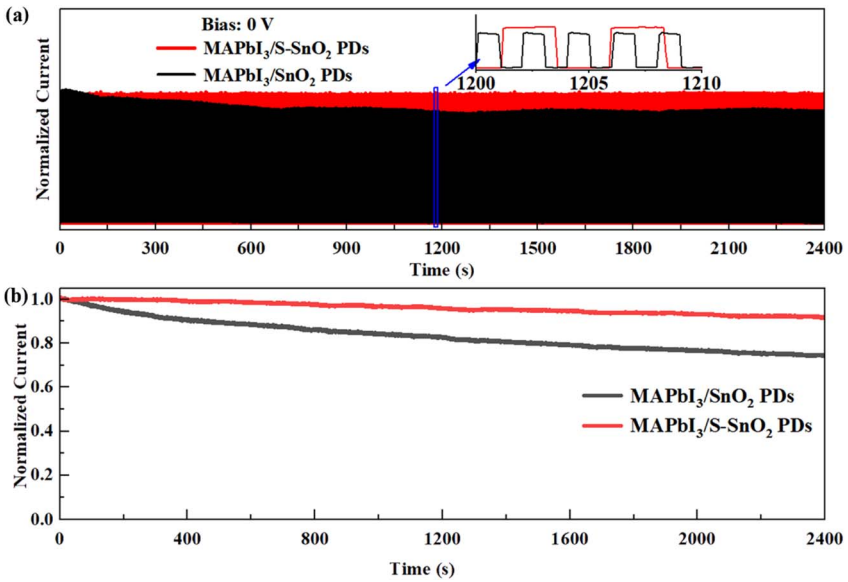

Fig. 6 Stability of photodetection of $MAPbI_3/SnO_2$ PDs. I–t curves captured (a) under pulsed illumination and (b) steady illumination.

In conclusion, surface engineering of SnO_2 with $(NH_4)_2WS_4$ has been demonstrated to effectively passivate the interfacial defects to fabricate improved $MAPbI_3/SnO_2$ PDs. It has been shown that the surface engineering with $(NH_4)_2WS_4$ resulted in S substituting for O lattice of SnO_2, which passivated the surface V_Os of SnO_2. Meanwhile, theoretical studies suggested that the S atoms at the surface of SnO_2 further suppressed the V_I and V_{Pb} at the bottom surface of $MAPbI_3$. Accordingly, the interfacial non-radiative recombination has been suppressed. On this basis, improved $MAPbI_3/SnO_2$ PDs have been fabricated, where the responsivity and detectivity of 0.41 A W^{-1} and 5×10^{12} Jones at the zero bias have been demonstrated. The results shown in this work pave the way for efficiently passivating the interfacial defects of LHP/SnO_2 heterojunctions in the future.

Conflicts of interest

The authors declare no conflict of interest.

Data availability

The data that support the findings of this study are available from the corresponding authors upon reasonable request.

Supplementary information (SI): experiments, and supporting figures including XRD and XPS results of SnO_2 and S-SnO_2 thin films, *I–V* curves of Au/SnO_2 (S-SnO_2)/ITO structures, supercells of $MAPbI_3$ containing various defects, and a photo image of $MAPbI_3/SnO_2$ PDs, statistical results of dark current and photocurrent of $MAPbI_3/SnO_2$ PDs treated with different $(NH_4)_2WS_4$, and supporting Tables for comparison of crystallinity of $MAPbI_3$ thin films prepared on SnO_2 and S-SnO_2. See DOI: https://doi.org/10.1039/d5ra10121b.

References

1 U. Khulal, J. Zhao, W. Hu and Q. Chen, Nondestructive quantifying total volatile basic nitrogen (TVB-N) content in chicken using hyperspectral imaging (HSI) technique combined with different data dimension reduction algorithms, *Food Chem.*, 2016, **197**, 1191–1199.
2 J. Sun, S. Jiang, H. Mao, X. Wu and Q. Li, Classification of Black Beans Using Visible and Near Infrared Hyperspectral Imaging, *Int. J. Food Prop.*, 2016, **19**(8), 1687–1695.
3 Q. Chen, W. Hu, J. Su, H. Li, Q. Ouyang and J. Zhao, Nondestructively sensing of total viable count (TVC) in chicken using an artificial olfaction system based colorimetric sensor array, *J. Food Eng.*, 2016, **168**, 259–266.
4 L. Wan, H. Li, C. Li, A. Wang, Y. Yang and P. Wang, Hyperspectral Sensing of Plant Diseases: Principle and Methods, *Agronomy*, 2022, **12**(6), 1451.
5 Y. Xu, M. M. Hassan, A. S. Sharma, H. Li and Q. Chen, Recent advancement in nano-optical strategies for detection of pathogenic bacteria and their metabolites in food safety, *Crit. Rev. Food Sci. Nutr.*, 2023, **63**(4), 486–504.
6 R. Wang, M. Mujahid, Y. Duan, Z.-K. Wang, J. Xue and Y. Yang, A Review of Perovskites Solar Cell Stability, *Adv. Funct. Mater.*, 2019, **29**(47), 1808843.
7 Z. Y. Zhang, L. Sun and G. P. Wang, Lateral Perovskite Single-Crystal Capacitors for Self-Powered Photodetection, *Adv. Electron. Mater.*, 2023, **9**(4), 2201318.
8 X. Shen, S. Yang, M. Chen, J. Su, J. Cai, P. Cheng, Y. Liu, Q. Wang and D. Cao, Interfacial Engineering with Aluminum Oxide toward an Improved Self-Powered Narrowband Visible-Light Photodetection in Lead Halide Perovskite $CH_3NH_3PbBr_3$/p-Si Heterojunctions, *Adv. Mater. Interfaces*, 2022, **9**(14), 2102305.
9 L.-J. Feng, Y.-Y. Zhao, R.-Y. Song and X.-W. Lei, Three homologous 1D lead halide perovskites with broadband white-light emissions, *Inorg. Chem. Commun.*, 2022, **136**, 109146.
10 P. C. Kumar, S. Mohanty, J. Panda, S. Das, S. Supriya, D. Alagarasan and R. Naik, Enhanced photoresponse in a Ag2S/In2Se3 heterojunction based visible light photodetector, *RSC Adv.*, 2025, **15**(18), 14518–14531.
11 L. Mahapatra, S. Supriya, P. C. Kumar, D. Alagarasan, C. Sripan and R. Naik, Increase in photo sensitivity and detectivity of Bi/Sb35S35Se30 heterostructure films upon time-dependent laser irradiation for photodetection, *Surf. Interfaces*, 2025, **72**, 107091.
12 K. Manjunatha, D. Alagarasan, S. Das, R. Ganesan, R. Naik, D. Purohit and M. Ramudu, Influence of substrate temperature on SnSe2/TiO2 heterostructure for photodetector applications, *Sens. Actuators, A*, 2025, **391**, 116641.
13 G. Mallick, P. C. Kumar, R. Naik and R. Biswal, Enhanced Photoresponse from Ag/Bi2Se3 Heterostructure Thin Films under Thermal Annealing, *ACS Appl. Electron. Mater.*, 2025, **7**(12), 5583–5598.
14 S. Kumaresan, I. Kathiravan, V. Vijendran and J. Balasundaram, Inorganic hole transport layer for lead free bismuth halide perovskite for photovoltaic device, *Opt. Mater.*, 2024, **154**, 115722.
15 J. Haddad, B. Krogmeier, B. Klingebiel, L. Krueckemeier, S. Melhem, Z. Liu, J. Huepkes, S. Mathur and T. Kirchartz, Analyzing Interface Recombination in Lead-Halide Perovskite Solar Cells with Organic and Inorganic Hole-Transport Layers, *Adv. Mater. Interfaces*, 2020, **7**(16), 2000366.
16 K. Ahmad and R. A. Khan, Improved photovoltaic performance of lead halide perovskite solar cells using spiro-OMeTAD plus CNTs as hole transport layer, *J. Mater. Sci. Mater. Electron.*, 2025, **36**(7), 425.
17 J. Kim, K. S. Kim and C. W. Myung, Efficient electron extraction of SnO_2 electron transport layer for lead halide perovskite solar cell, *npj Comput. Mater.*, 2020, **6**(1), 100.
18 L. Huang, X. Sun, C. Li, J. Xu, R. Xu, Y. Du, J. Ni, H. Cai, J. Li, Z. Hu and J. Zhang, UV-Sintered Low-Temperature Solution-Processed SnO_2 as Robust Electron Transport Layer for Efficient Planar Heterojunction Perovskite Solar Cells, *ACS Appl. Mater. Interfaces*, 2017, **9**(26), 21909–21920.
19 Z. Molenda, S. Chambon, D. M. Bassani and L. Hirsch, Electronic Doping in Perovskite Solar Cells, *Adv. Electron. Mater.*, 2024, **10**(10), 2400090.

20 J. Jeong, H.-B. Kim, Y. J. Yoon, N. G. An, S. Song, J. W. Kim, M. Kim, H. Jang, D. S. Kim, G.-H. Kim and J. Y. Kim, The introduction of a perovskite seed layer for high performance perovskite solar cells, *J. Mater. Chem. A*, 2018, **6**(41), 20138–20144.

21 X. Meng, J. Deng, Q. Sun, B. Zong, Z. Zhang, B. Shen, B. Kang, S. R. P. Silva and L. Wang, High-efficiency planar heterojunction perovskite solar cell produced by using 4-morpholine ethane sulfonic acid sodium salt doped SnO_2, *J. Colloid Interface Sci.*, 2022, **609**, 547–556.

22 P. Wang, B. Chen, R. Li, S. Wang, N. Ren, Y. Li, S. Mazumdar, B. Shi, Y. Zhao and X. Zhang, Cobalt Chloride Hexahydrate Assisted in Reducing Energy Loss in Perovskite Solar Cells with Record Open-Circuit Voltage of 1.20 V, *ACS Energy Lett.*, 2021, **6**(6), 2121–2128.

23 T. Bu, J. Li, F. Zheng, W. Chen, X. Wen, Z. Ku, Y. Peng, J. Zhong, Y.-B. Cheng and F. Huang, Universal passivation strategy to slot-die printed SnO_2 for hysteresis-free efficient flexible perovskite solar module, *Nat. Commun.*, 2018, **9**, 4609.

24 Z. Yang, Y. Deng, X. Zhang, S. Wang, H. Chen, S. Yang, J. Khurgin, N. X. Fang, X. Zhang and R. Ma, High-Performance Single-Crystalline Perovskite Thin-Film Photodetector, *Adv. Mater.*, 2018, **30**(8), 1704333.

25 X. Guo, J. Du, Z. Lin, J. Su, L. Feng, J. Zhang, Y. Hao and J. Chang, Enhanced efficiency and stability of planar perovskite solar cells using SnO_2:$InCl_3$ electron transport layer through synergetic doping and passivation approaches, *Chem. Eng. J.*, 2021, **407**, 127997.

26 Y. Zhao, L. Gao, Q. Wang, Q. Zhang, X. Yang, J. Zhu, H. Huang, J. Duan and Q. Tang, Reinforced SnO_2 tensile-strength and "buffer-spring" interfaces for efficient inorganic perovskite solar cells, *Carbon Energy*, 2024, **6**(6), e468.

27 Q. Feng and G. Nan, How Do A-Site Cations Regulate Trap States at Defective Surfaces of Lead Iodide Perovskites?, *J. Phys. Chem. Lett.*, 2022, **13**(21), 4831–4839.

28 Y. Rui, T. Li, B. Li, Y. Wang and P. Mueller-Buschbaum, Two-dimensional SnS_2 nanosheets as electron transport and interfacial layers enable efficient perovskite solar cells, *J. Mater. Chem. C*, 2022, **10**(34), 12392–12401.

29 J. Sun, Y. Gu, Y. Lu, J. Hu, T. Chen, C. Zhu and P. Luo, Synergistic strategy of rubidium chloride regulated SnO_2 and 4-butyl-benzylammonium iodide passivated MAxFA1-xPbI3 for efficient mixed-cation perovskite solar cells, *Chem. Eng. J.*, 2023, **468**, 143722.

30 L. Xiong, Y. Guo, J. Wen, H. Liu, G. Yang, P. Qin and G. Fang, Review on the Application of SnO_2 in Perovskite Solar Cells, *Adv. Funct. Mater.*, 2018, **28**(35), 1802757.

31 S. Das, S. Senapati, G. K. Pradhan, S. Varadharajanperumal and R. Naik, A Facile Microwave-Assisted Nanoflower-to-Nanosphere Morphology Tuning of CuSe1–xTe1+x for Optoelectronic and Dielectric Applications, *ACS Appl. Nano Mater.*, 2023, **6**(7), 5298–5312.

32 S. Giri, P. C. Kumar, S. Supriya, D. Alagarasan and R. Naik, Enhanced photodetectivity and responsivity in In10Se70Te15Bi5 film by time-dependent laser irradiation for photodetector applications, *RSC Adv.*, 2025, **15**(55), 46821–46837.

33 J. Liu, S. Li, S. Liu, Y. Chu, T. Ye, C. Qiu, Z. Qiu, X. Wang, Y. Wang, Y. Su, Y. Hu, Y. Rong, A. Mei and H. Han, Oxygen Vacancy Management for High-Temperature Mesoporous SnO_2 Electron Transport Layers in Printable Perovskite Solar Cells, *Angew. Chem., Int. Ed.*, 2022, **61**(26), e202202012.

34 Y. Ai, W. Liu, C. Shou, J. Yan, N. Li, Z. Yang, W. Song, B. Yan, J. Sheng and J. Ye, SnO_2 surface defects tuned by $(NH_4)_2S$ for high-efficiency perovskite solar cells, *Sol. Energy*, 2019, **194**, 541–547.

35 X. Tao, H. Chen, Y. Zhou, Q. Peng and Y. Ouyang, The formation energy and interaction energy of point defects in ZrC, *J. Nucl. Mater.*, 2021, **557**, 153235.

36 Z. Wang, M. A. Kamarudin, N. C. Huey, F. Yang, M. Pandey, G. Kapil, T. Ma and S. Hayase, Interfacial Sulfur Functionalization Anchoring SnO_2 and $CH_3NH_3PbI_3$ for Enhanced Stability and Trap Passivation in Perovskite Solar Cells, *Chemsuschem*, 2018, **11**(22), 3941–3948.

37 S. B. Hong, S. Kim and H. W. Choi, Improved Performance of Perovskite Deep-Ultraviolet Photodetector Using FAPb(I/Br)3 as Light Absorption Layer, *Coatings*, 2023, **13**(2), 341.

38 D. J. Shin, S. Kim and H. W. Choi, Effect of Methylammonium Iodide (MACl) on MAPbI3-Based Perovskite UV-C Photodetectors, *Appl. Sci.*, 2024, **14**(14), 6223.

39 W. Qu, S. Weng, L. Zhang, M. Sun, B. Liu, W. Du and Y. Zhang, Self-powered ultraviolet–visible–near infrared perovskite/silicon hybrid photodetectors based on a novel Si/SnO2/MAPbI3/MoO3 heterostructure, *Appl. Phys. Express*, 2020, **13**(12), 121001.

40 W. Song, J. Lv, J. Li, X. Huang, H. Duan, H. Qin, S. Ma, J. Wei, X. He and Z. Li, Picowatt-Sensitive and Air-Stable Heterojunction UV Photodetectors Enabled by Large-Grained CsCu2I3 Film via Microgap Thermal Sublimation, *ACS Photonics*, 2025, **12**(8), 4478–4488.

41 Y. Peng, D. Jiang, M. Zhao, Y. Duan, H. Wei, H. Li, Q. Liang and S. Wang, High-performance UV-visible photodetectors based on ZnO/perovskite heterostructures, *J. Alloys Compd.*, 2023, **965**, 171372.

42 H. Zhou, J. Mei, M. Xue, Z. Song and H. Wang, High-Stability, Self-Powered Perovskite Photodetector Based on a CH3NH3PbI3/GaN Heterojunction with C60 as an Electron Transport Layer, *J. Phys. Chem. C*, 2017, **121**(39), 21541–21545.

43 Y. Yuan, H. Tao, H. Wang, J. Liu, Y. Zhang, Q. Fu, H. Zhao, T. Di, H. Long and S. Yao, The effect of UVO treatment on TiO2-MAPbI3 heterostructure photodetector prepared in air atmosphere, *Mater. Sci. Semicond. Process.*, 2024, **172**, 108079.

44 T. Li, H. Wu, Y. Hao, F. Ma, P. Zhu, Z. Li, F. Li, J. Yu, M. Liu, C. Lei and T. Liang, High-Performance Broadband

Photodetectors Combining Perovskite and Organic Bulk Heterojunction Bifunctional Layers, *Crystals*, 2024, **14**(10), 868.

45 X. Xu, Z. Liu, W. Chen, Y. Chen, W. He and Y. Peng, Heteropoly Blue Modified SnO2 for Highly Efficient Perovskite-Based Photodetectors, *ACS Appl. Energy Mater.*, 2025, **8**(9), 6112–6120.

46 S. Fang and Y. H. Hu, Thermo-photo catalysis: a whole greater than the sum of its parts, *Chem. Soc. Rev.*, 2022, **51**(9), 3609–3647.